# Modelling Cephalopod-inspired Pulsed-jet Locomotion for Underwater Soft Robots

**F Renda**[1,2]**, F Giorgio-Serchi**[2]**, F Boyer**[3]**, C Laschi**[2]

1 Khalifa University Robotics Institute, Khalifa University, Abu Dhabi, UAE.
2 BioRobotics Institute, Scuola Superiore Sant'Anna, Pisa, Italy.
3 Institut de Recherche en Communication et Cybernetique de Nantes, Ecole des Mines de Nantes, Nantes, France.

E-mail: `federico.renda@kustar.ac.ae`, `f.giorgioserchi@sssup.it`, `frederic.boyer@mines-nantes.fr`, `cecilia.laschi@sssup.it`,

**Abstract.** Cephalopods (i.e. octopuses and squids) are being looked upon as a source of inspiration for the development of unmanned underwater vehicles. One kind of cephalopod-inspired, soft-bodied vehicle developed by the authors entails a hollow, elastic shell capable of performing a routine of recursive ingestion and expulsion of discrete slugs of fluids which enable the vehicle to propel itself in water. The vehicle performances were found to depend largely on the elastic response of the shell to the actuation cycle, thus motivating the development of a coupled propulsion-elastodynamics model of such vehicles. The model is developed and validated against a set of experimental results performed with the existing cephalopod-inspired prototypes. A metric of the efficiency of the propulsion routine which accounts for the elastic energy contribution during the ingestion/expulsion phases of the actuation is formulated. Demonstration on the use of this model to estimate the efficiency of the propulsion routine for various pulsation frequencies and for different morphologies of the vehicles are provided. This metric of efficiency, employed in association with the present elastodynamics model, provides a useful tool for performing a-priori energetic analysis which encompass both the design specifications and the actuation pattern of this new kind of underwater vehicles.

## 1. Introduction

In recent times, bioinspired aquatic propulsion has gained large recognition in the scientific community [1]. Among the numerous modes of bioinspired underwater locomotion, fish-like caudal and finned propulsion have gathered the largest interest, probably because of the relatively sound understanding of the physics involved in these specific locomotion strategies [2, 3, 4, 5]. This explains the number and variety of fish-mimicking robots which are nowadays being developed with the intent of investigating the intricacies of their respective modes of locomotion and the assets herein [6, 7, 8].

As opposed to fish-inspired flapping foil propulsion, the pulsed-jet propulsion of cephalopods (i.e. squid and octopuses) has only earned very limited recognition, despite the corroborated evidence of its assets. This swimming mode relies on a routine of consecutive periods of ingestion and expulsion of finite slugs of ambient water enabled by the reciprocal expansion and collapse of a chamber, the "mantle", composed of elastic tissues and muscle bundles [9]. Experiments on pulsed jets across nozzles have highlighted the association of this kind of discontinuous flow with the onset of toroidal vortex flow structures which contribute to generating more impulse than the one produced by comparable continuous jets [10]. The recognition that the geometrical features of the jet can be actively altered to increase the amount of thrust produced over a pulsation ([11, 12]) has fostered the efforts to design new pulsed-jet propelled aquatic vehicles [13, 14, 15].

Beside the benefit granted by vortex ring-aided thrust production, theoretical arguments seem to suggest that cephalopods also capitalize on a positive addition to thrust imparted by the body-shape variations which occur during the pulsed-jetting routine. Indeed, the shape change associated to the shrinkage of the mantle during the ejection phase of the pulsation can be proven to take part in enhancing the thrust via the recovery of added-mass energy [16]. In the effort to develop innovative underwater vehicles, the joint effect of vortex-ring aided thrust production and shape-change driven energy recovery should be exploited with the purpose of endowing new cephalopod-inspired submersibles with augmented maneuvering skills.

## 2. Cephalopod-inspired Soft Unmanned Underwater Vehicles

Given the yet unexploited potential inherent to cephalopod-like propulsion, the authors have designed and tested a series of prototypes trust-worthily inspired by these organisms (Fig. 1). In addition to the advantages derived from the swimming routine of cephalopods, this new kind of vehicles also benefit from being composed, for the most part, of elastic materials. The recourse to elastomers as the constituent materials in the manufacturing of these new kind of underwater robots provides them with the reduced risk of suffering or causing damage, the capability to adjust through cramped spaces and narrow apertures, the reduced weight and the intrinsic safety for the human operator working in close collaboration with the robot. These are few of the major assets where soft robots (as robots composed for a large extent by highly compliant materials are commonly referred to) stands out in marine as much as in terrestrial applications.

The prototypes of [17, 18, 19] propel themselves in water by executing a routine analogous to that of living cephalopods. The vehicles, one of which is portrayed in Fig. 1, consist of an elastic, hollow shell, similar to a collapsible bladder which, upon pulling by a series of cables distributed over the internal walls of the shell and actuated by a DC motor, undergoes periodic phases of deflation and inflation. In doing so, the vehicle recursively ejects and ingests fluid thus refilling the bladder and performing a succession of pulsed-jets in a closely resemblant fashion to what cephalopods do when they swim.
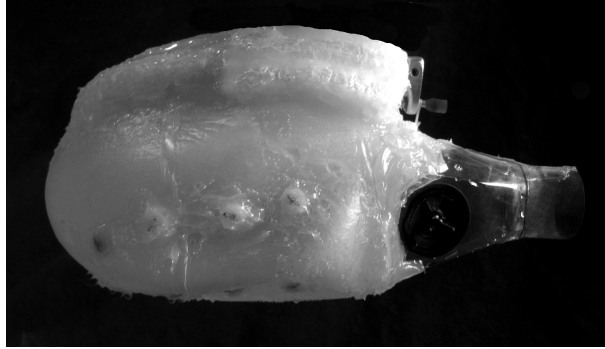
**Figure 1.** The Soft Unmanned Underwater Vehicle (SUUV) endowed with cable-driven pulsed-jet propulsion.

The actuation guided via cable-transmission deals with the collapse stage of the propulsion, while the inflation of the elastic cavity is regulated by the passive response of the rubber-like material which the shell is made of. In this regard, the vehicle is an underactuated system, where only half of the actuation cycle (i.e. the shell collapse, that is the fluid ejection stage) is actively controlled. By propelling themselves via the actual collapse of the elastic bladder, these underwater robots not only benefit of the advantages provided by vortex-ring aided thrust production, [12], but, upon adequate adjustment of their geometry, they could also capitalize on the positive feedback that added-mass recovery has upon thrust throughout the shape changing stage, [16].

The experiments performed by the authors on this kind of Soft Unmanned Underwater Vehicles (i.e. [17, 18, 19, 20]) show that their swimming performances is strongly dependent on the elastic response of the shell to the actuation routine, in particular during the inflation phase, as well as to the overall dynamics of the flexible vehicle in water. This gives rise to a complex, multifaceted problem of hydroelasticity. As a consequence of this, an integral characterization of the dynamics of such vehicles needs to take in consideration, on one hand, the reaction to the cable-driven pointwise actuation and, on the other hand, the passive inflation triggered by the emergence of the stresses within the thickness of the elastic shell during collapse. In this paper we introduce and test a formulation of an elastodynamics model for capturing the unsteady behaviour of the elastic shell throughout the actuation cycle and employ this model to simulate the vehicle dynamics during propulsion in water. Upon validation with existing experiments performed with the robotic prototype, the model is used to test new hypothetical designs of the vehicle.

## 2.1. Vehicle Design and Actuation

In the present work we will be taking into account the latest of the cephalopod-inspired prototypes developed, [19], see Fig. 1. In this vehicle, the actuation relies on cable transmission driven by a crank mechanism and a DC motor, see elements (3) and (2) in Fig. 2. The cables are fitted, at one end, to the internal side of the elastic

walls, elements (6) in Fig. 2, of the shell, gathered across an annular fixed pulley, element (1) in Fig. 2 and eventually linked, at the other end, to a crank the rotation of which cyclically pulls and releases the cables. The actuator is designed in such a way that, during half of the revolution of the crank, the cables are pulled radially inward, driving the displacement of the attachment points distributed over the inside of the shell. This enables the deformation of the shell, pressurizing the internal fluid and hence accelerating it through the nozzle. During the second half of the rotation of the crank, the cables are let loose, enabling the shell to inflate by passively exploiting the rigidity of its constituent material. This permits the refill of the shell with ambient fluid. The preference for a discrete, radially oriented, cable arrangement is motivated by the lower load torque needed for the crank mechanism to execute the collapse of the elastic shell and, at the same time, by the eased passive recovery of the inflated state of the mantle.
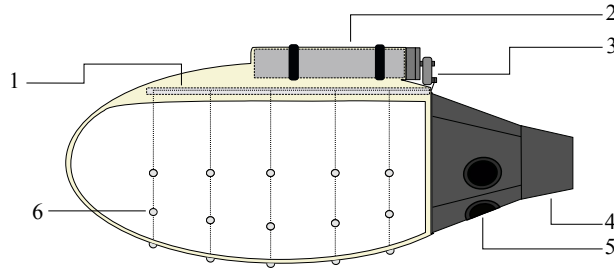


**Figure 2.** Schematic depiction of the prototype. The numbers refer to: (1) the axial fixed pulley, (2) the electric motor, (3) the crank, (4) the nozzle, (5) the ingestion valves and (6) the cable attachment points.

Upon assemblage, the vehicle, Fig. 1, consists of a hollow elastic shell of Smooth-On EcoFlex ®00-30 silicone. The actuation routine is guided by four groups of four nylon cables arranged over four cross sections along the shell, as schematically depicted in Fig. 2. The crank is fitted on to the shaft of a DC 441435 Maxon Motor. The nozzle is composed of a cylinder of flexible sheet sealed to the silicone walls and perforated on the side in order to fit three umbrella check valves which aid in the ingestion of water during the refill phase while at the same time preventing the leakage of water during the compression of the shell. The whole prototype, including electronic and mechanical components, weights 333.5 g, 212.0 g of which are silicone. The rigid components thus represent only the 36.5%, in mass, of the whole robot. Estimate of the expelled volume is achieved by measuring the volume of water stored within the mantle in strained conditions (i.e. when the mantle walls are contracted), which provides a value of 130 mL. This corresponds to 39% of the whole volume contained inside the mantle cavity under unstrained condition.

## 3. Mathematical Model of a Mobile Shell

Modelling soft locomotion system is a challenging issue which requires to conciliate continuous media and rigid body mechanics. In the recent past years a perspective based on the Cosserat model of continuous media, has been opened. The approach, which allows to capture in an homogeneous formalism both the rigid overall motions and the internal strains, has been applied through the model of Reissner beams, to the locomotion of continuous and soft elongated animals [21] and octopus soft arms manipulation [22]. Here, it is for the first time applied to a 2D medium by modelling the mantle like structure of our soft underwater robot as a Reissner axisymetric shell [23]. According to the Cosserat model, the shell is modelled as a continuous assembly of rigid fibers along the median surface of the shell. Adopting the Reissner model, the general configuration space of a shell as it appear in [23], can be reduced exploiting the axis symmetry of the soft robot. The details of this reduction are described below step by step, by generalizing for mobile shell the author's previous paper on hyperstatic shell [24, 25].

### 3.1. Kinematics

Mathematically, an axisymmetric surface or "surface of revolution", is obtained by rotating a planar curve or "profile" around a fixed axis named "symmetry axis". This rotation changes the "profile curve" of resting length $L$ into any of the meridian curves that constitute the shell. The ambient Euclidean space is endowed with a fixed base of orthogonal unit vectors $(\mathbf{e}_1, \mathbf{e}_2, \mathbf{e}_3)$, where $\mathbf{e}_3$ supports the symmetry axis (Fig. 3). Denoting by $\phi$ the angle of revolution and by $X$ the abscissa along the meridian, the orthogonal basis $(\mathbf{e}_r, \mathbf{e}_\phi, \mathbf{e}_3)$ fixed to the material point of coordinates $(\phi, X)$ is defined by roto-translating $(\mathbf{e}_1, \mathbf{e}_2, \mathbf{e}_3)$ of:

$$g_1 \in SE(3) : (\phi, X) \in [0, 2\pi[\times[0, L] \mapsto g_1(\phi, X) = \begin{pmatrix} \exp(\tilde{\mathbf{e}}_3\phi) & \mathbf{r} \\ 0 & 1 \end{pmatrix},$$

where exp is the exponential in SO(3) and the tilde is the usual isomorphism between a vector of $\mathbb{R}^3$ and the corresponding skew-symmetric matrix; $\mathbf{r} : (\phi, X) \in [0, 2\pi[\times[0, L] \mapsto \mathbf{r}(\phi, X) = (\cos(\phi)r(X), \sin(\phi)r(X), z(X))^T$ is a curve that define the profile of the shell and for which, $r(.)$ and $z(.)$ are two smooth functions which define the radius and the altitude of the point $X$ on the profile (see Figure 3). For the sake of convenience, we introduce another reference frame $(\mathbf{e}_r, \mathbf{e}_3, -\mathbf{e}_\phi)$ rotated from the former by

$$g_2 \in SE(3) : g_2 = \begin{pmatrix} \exp(\tilde{\mathbf{e}}_r\pi/2) & 0 \\ 0 & 1 \end{pmatrix}.$$

Then, if we call $\theta(X)$ the angle between $\mathbf{e}_3$ and the shell fiber located at any $X$ along the $\phi$-meridian, the so called *director orthogonal frame* $(\mathbf{a}, \mathbf{b}, -\mathbf{e}_\phi)$ is defined by:

$$g_3 \in SE(3) : X \in [0, L] \mapsto g_3(X) = \begin{pmatrix} \exp(-\tilde{\mathbf{e}}_\phi\theta) & 0 \\ 0 & 1 \end{pmatrix}.$$

Finally, putting them all together, the shell configuration space at each instant $t$ is

$$g \in SE(3) : g(\phi, X) = g_1 g_2 g_3 = \begin{pmatrix} R & \mathbf{r} \\ 0 & 1 \end{pmatrix},$$

where the rotation matrix $R$ have been defined as $R = \exp(\tilde{\mathbf{e}}_3 \phi) \exp(\tilde{\mathbf{e}}_r \pi/2) \exp(-\tilde{\mathbf{e}}_\phi \theta)$. As a result, we can now introduce the following definition of the configuration space of an axisymmetric shell:

$$\mathcal{C} := \{(\phi, X) \in B \mapsto g \in SE(3)\} \tag{1}$$

where, $B \subset S^1 \times \mathbb{R}$. Note that (1) defines equivalently the field of director frames over the entire shell.

Now we can define the tangent plane on the surface $g(\phi, X)$ spanned by the two vector fields: $\widehat{\xi}_1(X) = g^{-1} \partial g / \partial X = g^{-1} g'$ and $\widehat{\xi}_2(X) = g^{-1} \partial g / \partial(r^o \phi) = g^{-1} g^l$. The hat represents the isomorphism between the twist vector space $\mathbb{R}^6$ and the Lie algebra $se(3)$ and $r^o(X)$ is the value of $r(X)$ in the reference configuration of the shell (before any deformation). Below their components are specified in the director frames:

$$\begin{aligned} \xi_1 &= (\mathbf{k}_1^T, \mathbf{g}_1^T)^T = (0, 0, \mu, \lambda, \beta, 0)^T \in \mathbb{R}^6 \\ \xi_2 &= (\mathbf{k}_2^T, \mathbf{g}_2^T)^T = (\tfrac{\sin(\theta)}{r^o}, \tfrac{\cos(\theta)}{r^o}, 0, 0, 0, \tfrac{-r}{r^o})^T \in \mathbb{R}^6, \end{aligned} \tag{2}$$

where the curvature $\mu$ and the longitudinal and transversal strains $(\lambda, \beta)$ have been defined as $\mu = \theta'$, $\lambda = \cos(\theta) r' + \sin(\theta) z'$ and $\beta = \cos(\theta) z' - \sin(\theta) r'$.

The time evolution of the configuration surface $g$ is represented by the twist vector field $\eta(X) \in \mathbb{R}^6$ defined by $\widehat{\eta} = g^{-1} \partial g / \partial t = g^{-1} \dot{g}$. Let us specify the component of

$$\eta = (\mathbf{w}^T, \mathbf{v}^T)^T = (0, 0, \Omega, V_a, V_b, 0)^T \in \mathbb{R}^6,$$

where the angular velocity $\Omega$ and the longitudinal and transversal velocity $(V_a, V_b)$ in the directors frame have been defined as $\Omega = \dot{\theta}$, $V_a = \cos(\theta) \dot{r} + \sin(\theta) \dot{z}$ and $V_b = \cos(\theta) \dot{z} - \sin(\theta) \dot{r}$. Finally, from $\dot{g} = g\widehat{\eta}$, the kinematic equations are

$$\begin{aligned} \dot{\theta} &= \Omega \\ \dot{r} &= \cos(\theta) V_a - \sin(\theta) V_b \\ \dot{z} &= \sin(\theta) V_a + \cos(\theta) V_b \end{aligned} \tag{3}$$

### 3.2. Compatibility Equations

It has been shown above that $g' = g\widehat{\xi}_1$. By taking the derivative of this equation with respect to time and recalling that $\dot{g} = g\widehat{\eta}$, we obtain the following compatibility equation between the velocity and the deformation variables: $\dot{\widehat{\xi}}_1 = \widehat{\eta}' + \widehat{\xi}_1 \widehat{\eta} - \widehat{\eta} \widehat{\xi}_1$. In terms of twist vectors this can be written as:

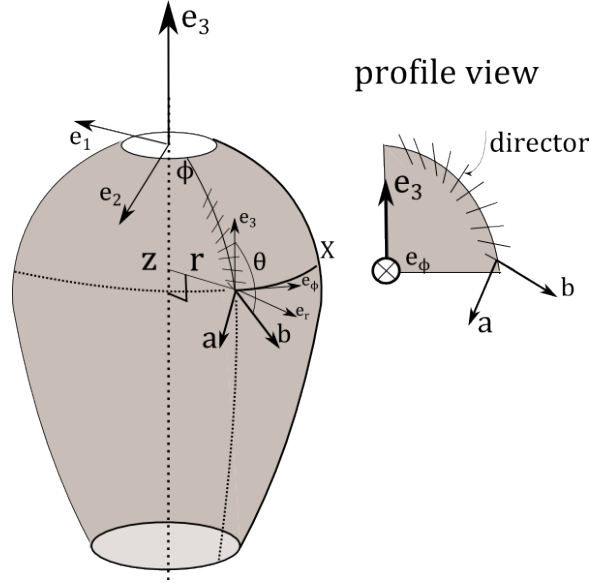$$\dot{\xi}_1 = \eta' + \mathrm{ad}_{\xi_1}(\eta), \tag{4}$$

**Figure 3.**     Axisymmetric shell kinematics (left).     Profile view, beam-like parametrization (right).

where ad is the adjoint map defined as in [25]. From (4), the compatibility equations are:

$$\begin{aligned}
\dot{\mu} &= \Omega' \\
\dot{\lambda} &= V_a' + \beta\Omega - \mu V_b \\
\dot{\beta} &= V_b' - \lambda\Omega + \mu V_a
\end{aligned} \tag{5}$$

### 3.3. Strain Measures

Before describing the strain measures, let us introduce two quadratic forms named: $h(X)$ and $k(X)$, that represent the first and the second fundamental forms of a Reissner shell, respectively.

    The first fundamental form is defined in each point $(\phi, X)$ of the surface by a tensor, the components of which are deduced from the scalar products of all the vectors of the field of basis (said natural basis) $(\mathbf{g}_1, \mathbf{g}_2)(\phi, X)$ (see (2)). For our surface of revolution it can be simply expressed as:

$$h_{11} = \lambda^2 + \beta^2 \qquad h_{22} = r^2/r^{o2},$$

which, due to the axisymmetry, depends only on $X$.

    For a Reissner shell, the components of the second fundamental form are such that $k_{\alpha\gamma} = \mathbf{g}_\alpha^T \widetilde{\mathbf{k}}_\gamma \mathbf{b}$ ($\alpha, \gamma \in \{1, 2\}$), thus we have:

$$k_{11} = -\mu\lambda \qquad k_{22} = -r\sin(\theta)/r^{o2}.$$

    Now, in accordance with [23], the strain tensor field which describes the membrane strain state in the mid-surface is $e(X) = 1/2(h - h^o)$, giving

$$e_{11} = 1/2(\lambda^2 + \beta^2 - 1) \qquad e_{22} = 1/2(r^2/r^{o2} - 1).$$

For what concerns the shear strain state, we use the strain vector $s_\alpha(X) = \mathbf{g}_\alpha^T \mathbf{b} - \mathbf{g}_\alpha^{oT} \mathbf{b}^o$, with components:

$$s_1 = \beta \qquad s_2 = 0,$$

while the flexural strain state is parametrized by the tensor field $d(X) = k - k^o$, with components:

$$d_{11} = \mu^o - \mu\lambda \qquad d_{22} = \sin(\theta^o)/r^o - r\sin(\theta)/r^{o2}.$$

In all the above definitions, the upper index $o$ represents a field when it is evaluated in the reference relaxed configuration. Furthermore, we have used $h_{11}^o = 1$, while it is natural to consider that there is no transverse shearing in the reference resting configuration, i.e. $\beta^o = 0$.

### 3.4. Dynamics

The p.d.e.'s describing the evolution of a generic Reissner shell (not necessarily axisymmetric) have been derived in [23]. With respect to the local reference frame, these p.d.e's can be written, in a geometric notation, as:

$$\mathcal{M}\dot{\eta} = 1/j(j\mathcal{F}_i^1)' + \mathrm{ad}_{\xi_\alpha}^*(\mathcal{F}_i^\alpha) + \mathcal{F}_e - \mathrm{ad}_\eta^*(\mathcal{M}\eta), \tag{6}$$

where $j = \sqrt{\det(h)} = r/r^o\sqrt{\lambda^2 + \beta^2}$, $\mathcal{F}_i^\alpha$ are the wrenches of internal forces in the surface directions given by $\mathbf{g}_\alpha$, $\mathcal{F}_e$ is the external wrench of distributed applied forces, $\mathcal{M}$ is the screw inertia matrix and $\mathrm{ad}^*$ is the co-adjoint map equal to $ad^* = -ad^T$. For the repeated $\alpha$ the Einstein convention has to be used as in the rest of the paper. Due to the axisymmetry, the internal and external wrench fields take the particular form ([26]):

$$\mathcal{F}_i^1(X) = (0, 0, M_X, N_X, H, 0)^T \in \mathbb{R}^6 \tag{7}$$

$$\mathcal{F}_i^2(X) = (M_\phi, 0, 0, 0, 0, -N_\phi)^T \in \mathbb{R}^6 \tag{8}$$

$$\mathcal{F}_e(X, t) = (0, 0, l, f_a, f_b, 0)^T \in \mathbb{R}^6 \tag{9}$$

and the screw inertia matrix is equal to: $\mathcal{M} = diag(\rho J, \rho J_b, \rho J, 2\rho h, 2\rho h, 2\rho h) \in \mathbb{R}^6 \otimes \mathbb{R}^6$. In the equations above $\rho$ is the body density, $h$ is the half of the shell thickness and $J$, $J_b$ are the second moment of the cross sectional fiber equal to $J = h^2/3$, $J_b \sim 0$.

In components, the dynamic equations are:

$$\begin{aligned}
\rho J\dot{\Omega} &= 1/j(jM_X)' + \lambda H - \beta N_X - \frac{\cos(\theta)}{r^o}M_\phi + l \\
2\rho h\dot{V}_a &= 1/j(jN_X)' - \mu H - \frac{\cos(\theta)}{r^o}N_\phi + f_a + 2\rho h\Omega V_b \\
2\rho h\dot{V}_b &= 1/j(jH)' + \mu N_X + \frac{\sin(\theta)}{r^o}N_\phi + f_b - 2\rho h\Omega V_a
\end{aligned} \tag{10}$$

### 3.5. Constitutive Equations

An extended formulation of a visco-elastic constitutive model based on the Kelvin-Voigt model, has been developed in [25], starting from the hyper-elastic isotropic model of [23] and the consideration for the viscous contribution of [27]. Below, the final equations for our axialsymmetric resultant stress-couple are reported:

$$N_X = \frac{2Eh}{1-\nu^2} \left[ \lambda \left( e_{11} + \nu e_{22} \right) - J\mu \left( d_{11} + \nu d_{22} \right) \right]$$
$$+ \frac{6vh}{1-\nu^2} \left[ \lambda \left( \dot{e}_{11} + \nu \dot{e}_{22} \right) - J\mu \left( \dot{d}_{11} + \nu \dot{d}_{22} \right) \right],$$

$$N_\phi = \frac{2Eh}{1-\nu^2} \left[ \frac{r}{r^o} \left( e_{22} + \nu e_{11} \right) - J\frac{\sin(\theta)}{r^o} \left( d_{22} + \nu d_{11} \right) \right]$$
$$+ \frac{6vh}{1-\nu^2} \left[ \frac{r}{r^o} \left( \dot{e}_{22} + \nu \dot{e}_{11} \right) - J\frac{\sin(\theta)}{r^o} \left( \dot{d}_{22} + \nu \dot{d}_{11} \right) \right],$$

$$H = 2h\beta \left[ G + \frac{E}{1-\nu^2} \left( e_{11} + \nu e_{22} \right) \right] + 2h\dot{\beta} \left[ v + \frac{3v}{1-\nu^2} \left( \dot{e}_{11} + \nu \dot{e}_{22} \right) \right], \tag{11}$$

$$M_X = -\frac{2EhJ}{1-\nu^2} \lambda \left( d_{11} + \nu d_{22} \right) - \frac{6vhJ}{1-\nu^2} \lambda \left( \dot{d}_{11} + \nu \dot{d}_{22} \right),$$

$$M_\phi = -\frac{2EhJ}{1-\nu^2} \frac{r}{r^o} \left( d_{22} + \nu d_{11} \right) - \frac{6vhJ}{1-\nu^2} \frac{r}{r^o} \left( \dot{d}_{22} + \nu \dot{d}_{11} \right),$$

where $\nu$ is the Poisson ratio, $E$ the Young modulus, $G = E/(2(1+\nu))$ the shear modulus and $v$ the shear viscosity modulus.

## 4. External Loads

The external loads exerted by the fluid taken into account are the generated thrust, the dissipative drag and the added mass effect. Furthermore, the active actuation load exerted by the cables is considered. Below, the positions of all these external loads with respect to equation (6) are shown.

$$\mathcal{F}_e(X, t) = (0, 0, 0, (\mathsf{d} + \mathsf{c} + \mathsf{t} + \mathsf{f})^T)^T, \tag{12}$$

where $\mathsf{d}$ is the drag, $\mathsf{c}$ is the added mass, $\mathsf{t}$ is the thrust and $\mathsf{f}$ is the actuation load. With (12), one can immediately deduced that the external torque $l$ in (9) is equal to zero.

The complete fluid-structure interaction dynamics evoked by the problem we are addressing is so far beyond the state of the art of the fluid dynamic community. In the rest of the article, we adopt a preliminary approach aiming at assessing the validity of our locomotion elastodynamic model of the mantle. To that end, we use the usual model of net external forces exerted on a rigid rocket (fig. 4), that we uniformly "rub on" the mantle. This allows one to derive a first "naive" model of the hydrodynamic forces (12) appearing in (10). Based on fluid dynamics inside and outside the mantle, a more realistic model of (12) is the subject of a work in progress.

*4.1. Fluid Forces Model*

The one-dimensional momentum equation for a neutrally buoyant, rigid body translating in water is,

$$\rho U_m \dot{V} = -\frac{1}{2}\rho_w C_d A_{ref} V|V| - B\rho U_m \dot{V} + q\rho_w \dot{U}, \tag{13}$$

where $U$ is the mantle inner volume, $U_m$ is the volume of the elastic material composing the shell mantle and $V$ is the swimming velocity. The first right hand side (RHS) term represents the drag, $C_d$ being the drag coefficient and $A_{ref}$ a reference area of the mantle; the second RHS term is the added mass, with $B$ being the axial added mass coefficient. The third term in eq. (13) is the thrust, given by the speed of the outflow $q$, with respect to the mantle, across the nozzle-exit area $A_n$ and the variation of mass $\rho_w \dot{U}$ occurring within the robot due to the collapse of the elastic chamber. The outflow speed is given by: $q = -C_f \dot{U}/A_n$, where $C_f$ defines a flow loss coefficient at the nozzle entrance, which is taken to vary between 0.6 and 1 [28]. The thrust term is thus rewritten as $q\rho_w \dot{U} = -\rho_w C_f \dot{U}|\dot{U}|/A_n$.

Comparing equation (13) with (10), the expression of the fluid force in the shell model can be found. To do so, we restrict the shell model to a one-dimensional momentum equation of a rigid body by (i) cancelling the internal forces along with the angular variables $(\Omega, \dot{\Omega}, l)$; (ii) integrating the two remaining translation equations and (iii) assuming the same linear variables $(V_a, V_b, f_a, f_b)$ to be constant for every point of the mantle. After (i)-(ii) and thanks to the axisymmetry of the system, which allows us to cancel the sum of the components on $\mathbf{e}_1, \mathbf{e}_2$ as well as the sum of the momentum generated by the linear forces, we end up with one single equation along $\mathbf{e}_3$, which reads:

$$\rho 2h \int\limits_0^{z(L)} \int\limits_0^{2\pi} \ddot{z} r d\phi dz = \int\limits_0^{z(L)} \int\limits_0^{2\pi} f_3 r d\phi dz,$$

where $f_3$ has been defined as: $f_3 = f_a \sin(\theta) + f_b \cos(\theta)$.

Now, using the condition (iii) and identifying $\dot{z}$ with $V$, we have

$$\rho U_m \dot{V} = f_3 A_m, \tag{14}$$

where $U_m = 2hA_m$ is the mantle volume and $A_m$ is the mantle area equal to $A_m = -\int_0^{z(L)} 2\pi r dz = -2\pi \int_0^L rz' dX$. Comparing equation (13) with (14), the expression of the fluid forces directed along $\mathbf{e}_3$ and acting on the mantle yield:

$$f_3 = -\frac{\rho_w C_d A_{ref} V|V|}{2A_m} - B\rho 2h\dot{V} - \frac{\rho_w C_f \dot{U}|\dot{U}|}{A_n A_m} \tag{15}$$

which can be used to define the vector of the fluid force of (12) as follows.

*4.1.1. Drag* The drag load is simply the first right term of (15) expressed with respect to the director orthogonal frame, thus:

$$\mathsf{d} = R^T(0, 0, -\frac{\rho_w C_d A_{ref} V|V|}{2A_m})^T, \tag{16}$$

where, in terms of the configuration variable $r(X)$, the reference area $A_{ref}$ is equal to $\pi(max(r))^2$. The swimming velocity $V$ is calculated at every time step as the average of the scalar field $\dot{z}(X)$, *i.e.* $V = (1/A_m) \int_o^{z(L)} \int_0^{2\pi} \dot{z} d\phi dz$.

*4.1.2. Added mass* For the added mass it is not possible to calculate $\dot{V}$ as the average of the scalar field $\ddot{z}(X)$, since this field is not derivable from the actual state vector. Nevertheless, the global effect of the added mass on the body can be obtained equivalently by implementing the added mass model of (15) to the vector field $\dot{\mathbf{v}}(X)$, thanks to the linearity of the model. This can be show with the following chain of equivalence:

$$-B\rho U_m \dot{V} = -B\rho U_m \frac{\int\limits_o^{z(L)} \int\limits_0^{2\pi} \ddot{z} r d\phi dz}{A_m} = -B\rho 2h \int\limits_o^{z(L)} \int\limits_0^{2\pi} [\sin(\theta)\dot{V}_a + \cos(\theta)\dot{V}_b] r d\phi dz =$$

$$-\int\limits_o^{z(L)} \int\limits_0^{2\pi} [\sin(\theta)(B\rho 2h \dot{V}_a) + \cos(\theta)(B\rho 2h \dot{V}_b)] r d\phi dz$$

where the first formula represents total added mass load of (13) and the last formula represents the resulting RHS after applying (i) and (ii) on equations (10), with $f_a = -B\rho 2h\dot{V}_a$ and $f_b = -B\rho 2h\dot{V}_b$. Hence, the added mass load is:

$$\mathbf{c} = -B\rho 2h\dot{\mathbf{v}} = -B\rho 2h(\dot{V}_a, \dot{V}_b, 0)^T \tag{17}$$

*4.1.3. Thrust* The thrust load is simply the last right term of (15) expressed with respect to the director orthogonal frame:

$$\mathbf{t} = R^T (0, 0, -\frac{\rho_w C_f \dot{U}|\dot{U}|}{A_n A_m})^T \tag{18}$$

where the time derivative of the mantle inner volume is:

$$\dot{U} = -\pi \int\limits_0^L (2r\dot{r}z' + r^2\dot{z}')dX$$

with

$$z' = \sin(\theta)\lambda + \cos(\theta)\beta, \qquad \dot{z}' = \sin(\theta)(\dot{\lambda} - \Omega\beta) + \cos(\theta)(\dot{\beta} + \Omega\lambda)$$

Given the orientation chosen in the kinematics of fig. 3, $z'$ result to be negative, which justifies the minus sign in the integral above.

## 4.2. Actuation Load

The rhythmic actuation provided by the cables can be modelled by taking the radial (along $\mathbf{e}_r$) force $f_r(X, t)$ as a $T$-periodic function with two phases: a contraction phase
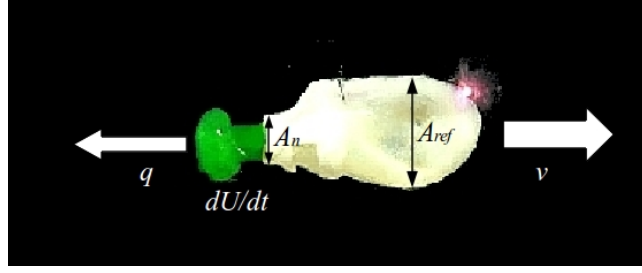
**Figure 4.** Depiction of the elements accounted for in the fluid dynamics model.

and a relaxation phase. The actuation pressure $f_r(X, t)$ has been taken equal to zero for all the $X$ except for a central interval of application $[\bar{X}, \bar{\bar{X}}]$. At these points $f_r(X, t)$ has been modelled as the ratio of the sum of the cable tension $(F(t))$ and the surface of the area of application: $f_r(X, t) = F(t)/\int_{\bar{X}}^{\bar{\bar{X}}} 2\pi r(X) z' dX$. The equation (19) shows the resultant actuation load vector used in this model, where the radial force is expressed with respect to the director orthogonal frame.

$$\mathsf{f} = R^T (\cos(\phi) f_r, \sin(\phi) f_r, 0)^T \tag{19}$$

## 5. Cephalopod-inspired Locomotion Model

Now we can state the system of second order partial differential equations by gathering the kinematics equations (3), the compatibility equations (5) and the dynamic equations (10), respectively complemented with the internal stresses (11) and the external loads (18), (16), (17) and (19). In the state-space form $\dot{x} = f(x, x', x'', t)$ the axisymmetric shell model is:

$$
\begin{aligned}
\dot{\theta} &= \Omega \\
\dot{r} &= \cos(\theta) V_a - \sin(\theta) V_b \\
\dot{z} &= \sin(\theta) V_a + \cos(\theta) V_b \\
\dot{\mu} &= \Omega' \\
\dot{\lambda} &= V_a' + \beta\Omega - \mu V_b \\
\dot{\beta} &= V_b' - \lambda\Omega + \mu V_a \\
\dot{\Omega} &= \frac{(jM_X)'/j + \lambda H - \beta N_X - \cos(\theta) M_\phi / r^o}{\rho J} \\
\dot{V_a} &= \frac{(jN_X)'/j - \mu H - \cos(\theta) N_\phi / r^o + 2\rho h \Omega V_b + f_a(t)}{2h(\rho + \rho B)} \\
\dot{V_b} &= \frac{(jH)'/j + \mu N_X + \sin(\theta) N_\phi / r^o - 2\rho h \Omega V_a + f_b(t)}{2h(\rho + \rho B)}
\end{aligned} \tag{20}
$$

where the second order partial differentiation appear from the viscosity component of the constitutive equation.

The system (20) is a non-autonomous system with an input explicitly dependent on time, represented by the cable tension $F(t)$. This, in turn, determine the external pressure $f_r(X, t)$ (19) which can be decomposed along the local references $(\mathbf{a}, \mathbf{b})$ and add to the passive (fluid) components of $f_a(t)$ and $f_b(t)$ (12). Then, the dynamics of (20), is able to generate the whole motions and deformations of the shell, both relative and absolute, without distinctions, thanks to the geometrically exactness of the approach.

## 5.1. Boundary Conditions

At both boundaries we have the following dynamic condition:

$$N_X(0) = f_{a,-} \qquad H(0) = f_{b,-} \qquad M_X(0) = -l_-$$
$$N_X(L) = f_{a,+} \qquad H(L) = f_{b,+} \qquad M_X(L) = -l_+ \tag{21}$$

where $f_{a+}$ $f_{a-}$, $f_{b+}$, $f_{b-}$, $l_+$ and $l_-$ denote the external forces along $\mathbf{a}$, $\mathbf{b}$ and torque along $-\mathbf{e}_\phi$, applied onto the sharp boundaries.

## 5.2. Numerical and Computational Aspects

In these forward dynamics, the state vector $x$ is infinite dimensional since all its components (along with those of $f$) are some functions of the profile abscissa $X$. As a result, the above state equation has to be first space-discretised on a grid of nodes along $[0, L]$ before being time integrated using explicit or implicit time integrators starting from the initial state $x(0)$. In this grid, all the space derivatives appearing in the $f$ vector can be approximated by finite difference schemes, while the external and internal stress forces and couples are respectively given by (16), (17) and the constitutive law (11). The system (20) is solved in Matlab$^\text{©}$ through an explicit second-order finite-difference scheme. On an AMD Phenom(TM) II X4 965 processor, at 784 Mhz, 3.25 GB of RAM it takes almost 204 sec for one second of simulation and a space resolution of 1.6% of the total length.

## 6. Experimental Validation

Tests performed on the robotic prototype are employed for validation of the shell model, in addition to the steady-state experiments conducted in [29]. The data acquired from the experimental apparatus provide us with information concerning the kinematics of the vehicle in water as well as on the energetics of the propulsion routine. The experiments are executed by recording the self-propulsion of the vehicle and by monitoring electric current flow across the DC motor. This quantity permits the derivation of the transient torque delivered by the shaft of the motor, hence enabling the inference of the force exerted by the cables for driving the shell collapse throughout the propulsion cycle. This data is of importance in determining the external loads condition in the elastodynamics model as far as eq. (19), $f_r(X, t)$ and $F(t)$ are concerned. In addition, vehicle displacement in time is recorded to derive the axial velocity profile in order to validate model results *a-posteriori*. The experimental setup and the data treatment are illustrated below.

## 6.1. Tank Testing

The experiments are performed in a 1150 mm long, 590 mm wide and 500 mm deep tank filled with tap water. The vehicle, Fig. 1, is allowed to travel along a straight line inside the tank by providing the motor with a constant voltage. This leads the motor to revolve

at a quasi-constant angular velocity, while at the same time undergoing oscillations in the electric current supply. The vehicle, floating at a depth proximal to the free surface, is allowed to slide along a wire held at the distal sides of the tank. The tests consist in recording the vehicle displacement in time as it travels from one end of the tank to the other. Tests are performed at 0.87, 1.12 and 1.22 pulsations per seconds (pps).

In the absence of a steerable nozzle, the wire helps the robot maintain a straight line during experimentation without exerting any appreciable friction. The major drawback of this setup lies in the oscillation of the vehicle as a result of the discontinuous accelerations due to the pulsed propulsion as well as the onset of a distinctive pitching moment arising from the ingestion and expulsion of fluid. Despite these source of moderate perturbation, experiments manifested a high degree of repeatability. The tests are recorded with a digital camera at 25 fps and subsequently treated with an image tracking software and a Savitzky-Golay low-pass filter to process the displacement and in this way derive the velocity temporal profiles. The axial component of the velocity will later be employed for comparison with the model results.

In addition, from the recordings of electric current, the tension of the cable bundle at the crank is derived; this is taken as the input force in the elastodynamics model. The electric current supplied to the motor throughout the pulsation cylce was measured in the case of a forcedly stationary prototype. This grants that the dynamic effect of the external flow during vehicle displacement could not affect the load acted upon the shell during actuation. A short section of the recordings of the cable tension pattern during actuation of the prototype is shown in Figure 5.
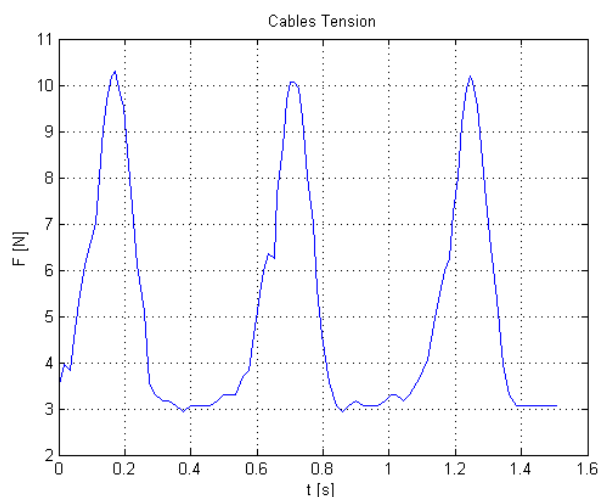


**Figure 5.** Cables tension of a forcedly not moving prototype with a motor frequency of 2 *pps*.

**Table 1.** Model Parameters

| Parameter | Value |
|---|---|
| $L$ | 138 $mm$ |
| $h$ | 1 $mm$ |
| $R$ | 31 $mm$ |
| $A_n$(outflow) | 491 $mm^2$ |
| $A_n$(inflow) | 1400 $mm^2$ |
| $E$ | 40 $KPa$ |
| $\nu$ | 0 |
| $\upsilon$ | 500 $KPa * s$ |
| $X1$ | 50 $mm$ |
| $X2$ | 130 $mm$ |
| $\rho$ | 7415 $Kg/m^3$ |
| $\rho_w$ | 1022 $Kg/m^3$ |
| $C_d$ | 1.7 |
| $B$ | 1.1 |
| $C_f$ | 1 |

*6.2. Underwater Locomotion Comparison*

In order to assess the comparison between the mathematical model and the experiments, the shell model developed in section 3 has been adopted to the working condition and geometrical properties of the experimental setting. The geometry of the mantle has been represented with an half sphere with a radius $R = 31$ $mm$ glued with a cylinder of length 92 $mm$, for a total profile length of $L = 138$ $mm$. The input of the model are the measured cable tension processed as explained in section 4.2, distributed over a central segment of 80 $mm$, with the period $T$ being the inverse of the motor frequency of the experiments. Since the boundary loads are not significant, the boundary conditions, eq. (21), have been set to zero. The distance between the real and the simulated swimming velocity $V$ has been minimized by applying a manual parameters identification procedure for the external loads coefficients $C_d$, $B$ and $C_f$, while the mechanical properties, i.e. the young modulus, has been manually calibrated in the model in order to achieve the experimentally measured volume contraction of 130 $ml$. The remaining geometrical parameters have been measured directly from the prototype. The model setting is summarized in Table 1.

The results of the comparison for the three motor frequencies are shown in Fig. 6. The distance between the two values has been evaluated with respect to the mean swimming velocity $\bar{V}$, thus the error is defined as: $e = |\bar{V} - \bar{V}^*|/\bar{V}^*$, where $\bar{V}^*$ is the average experimental swimming speed. The error for the three experiments are 3.8 %, 9.1 % and 18.2 % respectively from the slowest (0.87 $pps$) to the fastest (1.22 $pps$) case. For a qualitative comparison between the experimental and the simulated case, a
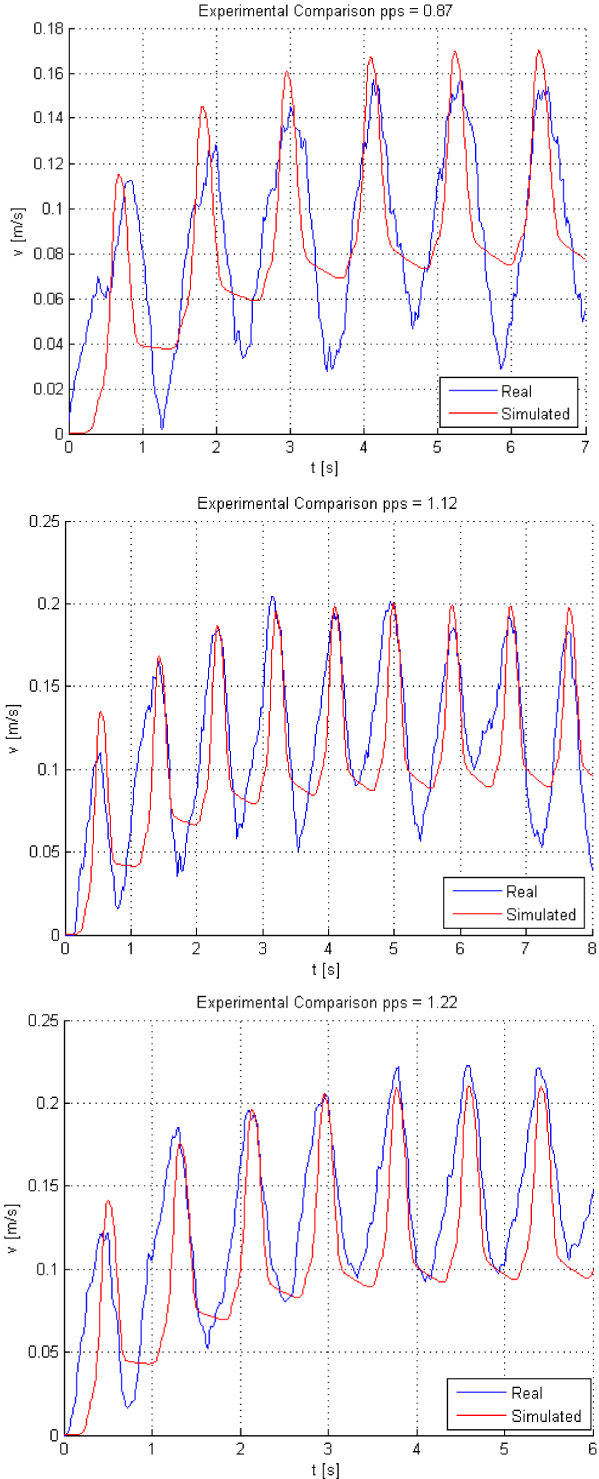
**Figure 6.** Real and simulated swimming velocity of the vehicle for tests performed at 0.87, 1.12 and 1.22 pulsation per seconds (pps).

series of video snapshots from the test performed at 1.12 pps is shown in Fig. 7. The full video is presented in the media file attached to this paper.
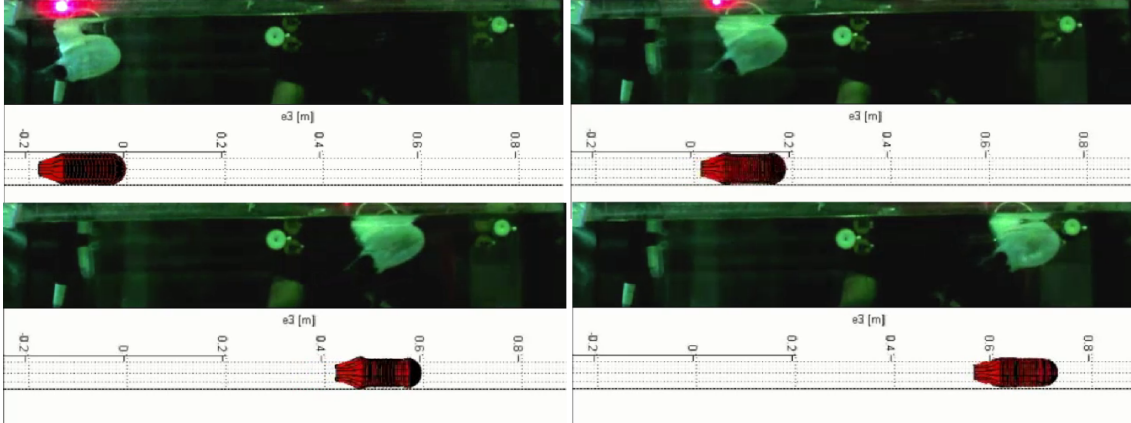


**Figure 7.**  Few snapshots of the real and simulated video of the swimming mantle with a motor frequency of 1.12 pps ran in parallel.

### 6.3. Discussion

The principal drawbacks and source of error of the present model is that we overcame the complexity of the natural fluid-structure problem by just "rub on" homogeneously on the surface of the deformable shell the well known solution of the one-dimensional momentum equation for a neutrally buoyant, rigid body translating in water (fig. 4). Furthermore, the axisymmetry assumption is a strong limitation over the possible geometries that could be simulated and in particular over the field of actuation load that could be applied. Indeed, even if the mantle shape of the prototype is actually axisymmetric, it is not rigorously the case of the cable actuation load which is not homogeneously distribute over the strip of coordinates $(X, \cdot)$. Nevertheless, the present model represents a step forward in the study of soft robots performing pulsed-jet locomotion, which is confirmed by the good results achieved.

### 7. Cephalopod-inspired Locomotion Analysis

Any kind of locomotion is the result of the dynamic interaction between the body deformation and the environment [30]. The quality of this interaction can be measured by calculating how a variation in time of the internal elastic energy of the body is translated into the thrust power of the motion. In this section such an energetic analysis is conducted, in order to measure the efficiency of the locomotion of our cephalopod-inspired soft unmanned underwater vehicle. This is probably the killer application of the model presented. To do so, we resort to the following efficiency index computed at each time step throughout the simulation:

$$\epsilon = \frac{W_t}{W_e} \tag{22}$$

where $W_t$ and $W_e$ respectively represent the thrust and elastic power. Following [31], those power can be calculated as

$$W_t = \int\limits_0^L \int\limits_0^{2\pi} (\mathsf{t} \cdot \mathsf{v})(-z')r d\phi dX$$

$$W_e = \int\limits_0^L \int\limits_0^{2\pi} \{\frac{2Eh}{1-\nu^2}[E_{11}\dot{E}_{11} + E_{22}\dot{E}_{22} + J(D_{11}\dot{D}_{11} + D_{22}\dot{D}_{22})] + 2hG\beta\dot{\beta}\}(-z')r d\phi dX$$

where $E_{11} = e_{11} + \nu e_{22}$, $E_{22} = e_{22} + \nu e_{11}$, $D_{11} = d_{11} + \nu d_{22}$ and $D_{22} = d_{22} + \nu d_{11}$. In Fig. 8, the elastic and thrust power respectively corresponding to the three experiments of Fig. 6 are shown.

In order to calculate a mean efficiency term and compare it among different tests, we resort to a suitable integral index for the cephalopod-inspired underwater locomotion which accounts for the ingestion and expulsion phases of the pulsed-jetting cycle. First, we take in consideration the steady regime of the locomotion alone, i.e. once the transient phase of acceleration of the vehicle has ceised. Then, we account for the fact that each pulsation comprises of an acceleration (i.e. the mantle contraction) and a deceleration (i.e. the mantle relaxation) phase. The net efficiency over a pulsation period is thus defined as the time averaging of the efficiencies from both the contributions, that is:

$$\eta = \frac{\int\limits_0^{t_c} \epsilon dt - \int\limits_{t_c}^{t_r} \epsilon dt}{T} \tag{23}$$

where $t_c$ and $t_r$ are respectively the contraction and relaxation time. Let us call $\eta$ the pulsation efficiency. A cephalod-inspired soft robot should be designed in order to maximize this index. For the cases accounted for we obtain $\eta$ equal to 7.1 %, 11 % and 13 % respectively for the 0.87, 1.12 and 1.22 pps cases. This highlights a trend according to which an increase in efficiency is associated with an increase in the pulsation frequency. This result is not surprising since, according to the propulsion model, thrust is proportional to the rate of change of the cavity volume. Therefore, at constant refill time governed by the passive elasticity, an increase of the actuation frequency leads to a faster variation of the cavity volume during the contraction phase and hence to higher thrust.

While this result is fairly intuitive and the model makes use of a coarse parameterization for the internal and external flow dyanmics, it nonetheless offers the chance to expand significantly on the characterization of the actuation routine for this new kind of soft-bodied, underactuated, pulsed-jet vehicles. This is done by accounting for the additional degree of freedom represented by the refill time and the parameters it depends on: the shell local curvature (i.e. the shape and size of the vehicle) and the Young modulus of its constituent material. In summary, the model enables to describe the mechanical properties of the vehicle which affect the actuation routine by
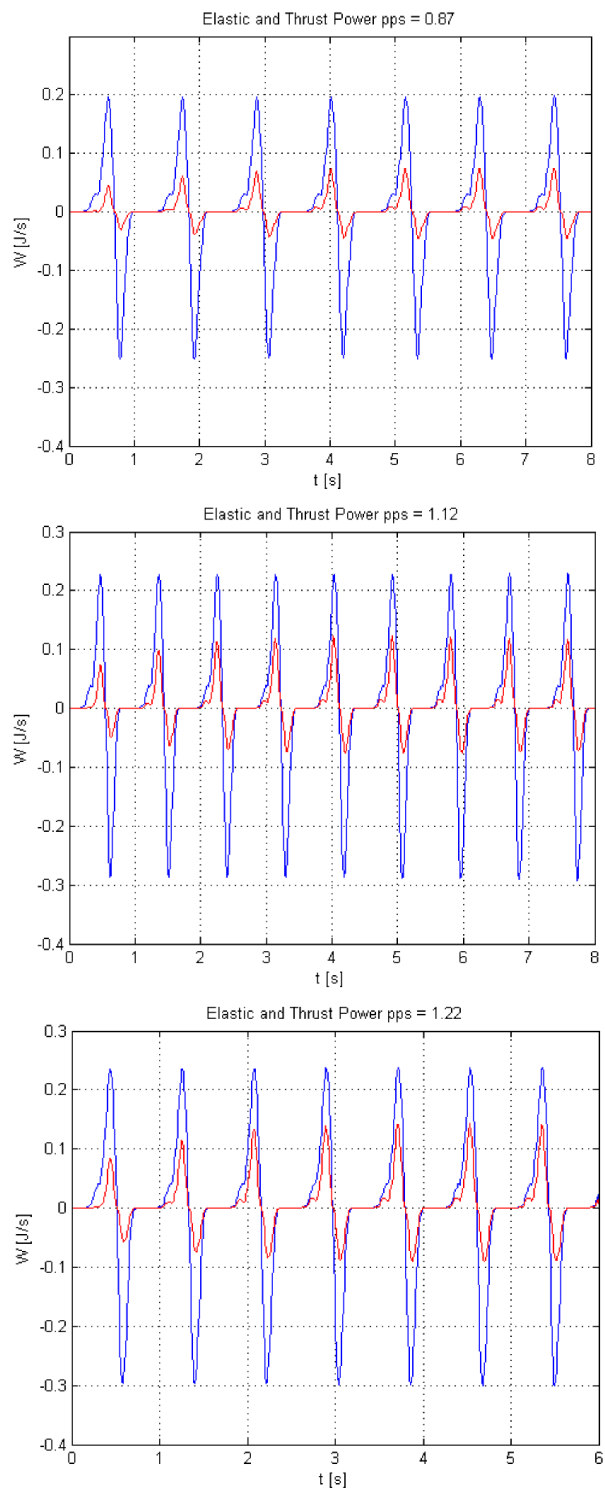
**Figure 8.** Elastic (blu) and thrust (red) power for three simulations in the same conditions of the experiments of Fig. 6.

determining the force required to collpase the shell, the final shape of the shell after deformation (and hence the amount of expelled fluid) and the refill time (which, in turn, regulates the maximum actuation frequency). An example of how the model can be used to explore different design parameters is illustrated in the following section.

### 7.1. Efficiency dependence on vehicle shape design

By relying on the metric for efficiency estimation employed in section 7, we demostrate the aptness of the present model to characterize the energetic balance of a new soft robot with a different morphology (Fig. 9). Here the radius of the sphere is set to 36 $mm$ while the length of the cylinder is decrased to 59 $mm$, with respect to the earlier test. This preserves the initial inner volume of 340 $ml$, thus granting a consistentcy of metrics for ease of comparison between the earlier and present simulations. All the other parameters are kept unchanged, with the exception of the geometrical location of the points $(\bar{X}, \bar{\bar{X}})$ which identify the segment of the shell subject to the actuation load. The new profile length is effectively shorter $(L = 112 \ mm)$ than the one of section 6.2, thus requiring us to adjust the loading segment in order to preserve the consistency among the tests. As a result, we set $\bar{X} = 28 \ mm$ and $\bar{\bar{X}} = 108 \ mm$. The thrust and elastic power for the three actuation frequencies accounted for in experiments of section 6.2 are shown in Figure 10.
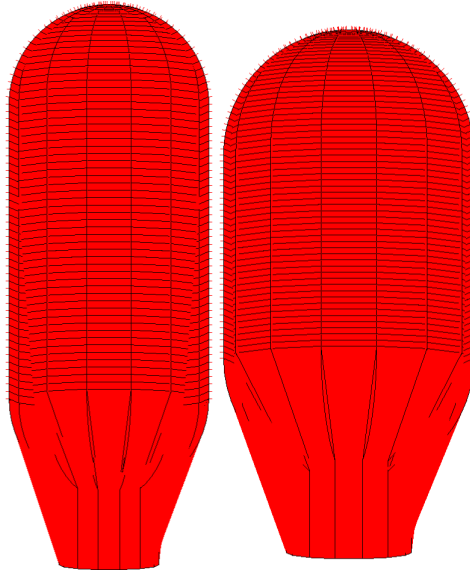


**Figure 9.** Original morphology of the shell (left) and the modified version of the efficiency test (right).

Estimation of $\eta$ yields values of 8.5 %, 13.3 % and 12.6 % respectively for the 0.87, 1.12 and 1.22 pps cases. We observe that, with respect to the previous set of tests (section 7), the pulsation efficiency is higher for the first two frequency and lower for the last. This can be explained by the fact that the volume contraction is higher by almost 30 $ml$, leading to an higher volume rate and consequently to an higher thrust (eq.
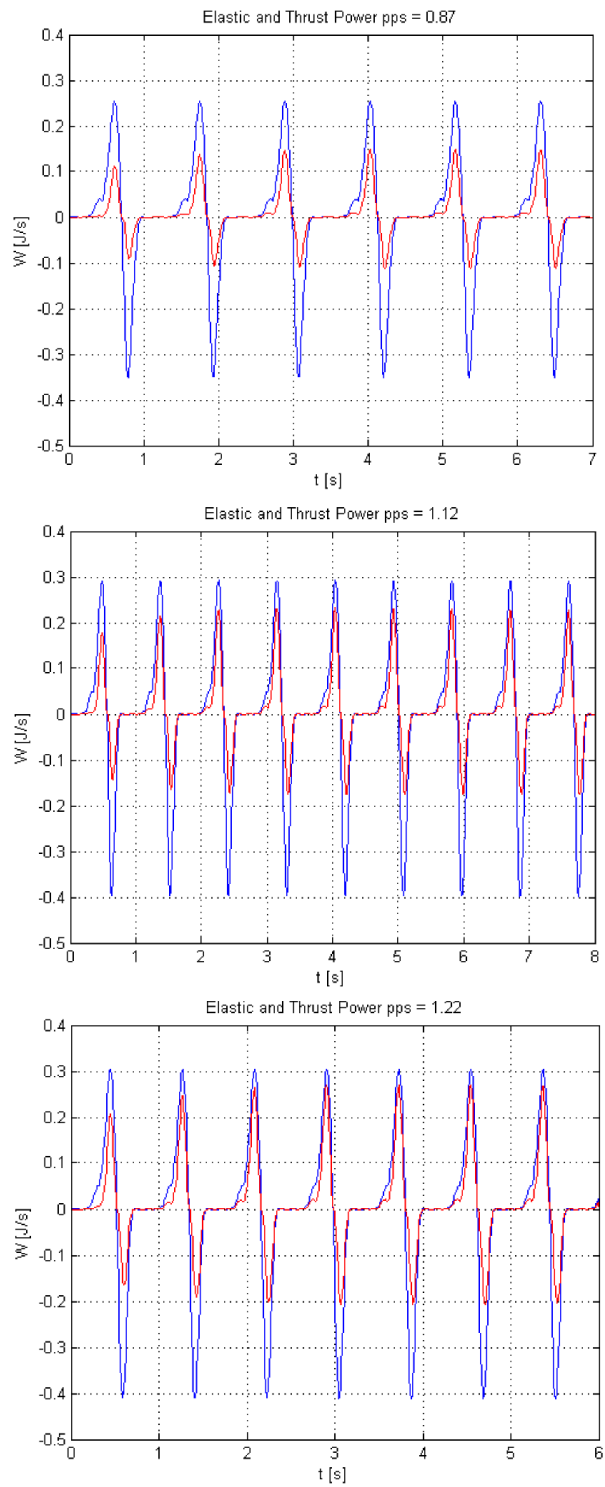
**Figure 10.** Elastic (blu) and thrust (red) power for three simulations in the same conditions of the experiments of section 6.2 except for the morphology that is modified as in Fig 9.

(18)) and efficiency. This efficiency improvement is compensated, for the last pulsation frequency, by the higher drag load, which is controlled by the larger reference area of the modified morphology (eq. (16)). As a matter of fact, it is worth to notice here that the competing thrust and drag loads are respectively linear w.r.t. the volume rate and quadratic w.r.t. the swimming velocity, leading to the non-monotonic relationship between frequency and efficiency found for the modified morphology, which indeed has an higher drag gain. Furthermore, uncontrolled elastodynamic effects, increasing the elastic power in a useless way, have been observed for the modified morphology at high pulsation frequency.

## 8. Conclusion

A geometrically exact elastodynamics model based on Cosserat theory is developed and coupled with the propulsion model for pulsed-jetting, rigidly translating bodies in water. The model is employed to simulate the dynamics of the soft-bodied, pulsed-jet vehicles developed by the authors and previously tested in controlled environments. Validation of the model against existing experiments of freely swimming, cephalopod-inspired vehicles in water brings evidence of its suitability at describing the shell dynamics throughout the active and passive stages of the actuation routine. Along with the coupled propulsion-elastodynamics model of the vehicle, a simple metric for the estimation of the propulsion efficiency of the underactuated system taken in consideration is devised. This metric accounts for both the contraction and refill phases of the propulsion routine and, when associated with the present elastodynamics model, yields an accurate quantification of both the design-dependent and actuation-dependent contributions. These tools provide invaluable support in the prediction and a-priori evaluation of the optimal design criteria and modes of operation of the new breed of underwater robots developed by the authors.

### Acknowledgment

### References

[1] P.R. Bandyopadhyay, "Trends in Biorobotic Autonomous Undersea Vehicles", *IEEE Journal of Oceanic Engineering*, vol. 30, 2005.
[2] M.J. Lighthill, "Note on the swimming of slender fish", *Journal of Fluid Mechnics*, vol. 9, 1960.
[3] T.Y-T Wu, "Hydrodynamics of swimming propulsion. Part 3. Swimming and optimum movements of slender fish with side fins", *Journal of Fluid Mechanics*, vol. 46, 1971.
[4] D.S. Barrett, M.S. Triantafyllou, D.K. P. Yue, M.A. Grosenbaugh, M.J. Wolfgang, "Drag reduction in fish-like locomotion", *Journal of Fluid Mechanics*, vol. 392, 1999.
[5] M.S. Triantafyllou, G.S. Triantafyllou and D.K.P. Yue, "Hydrodynamics of fish-like swimming", *Annual Review of Fluid Mechanics*, vol. 32, 2000.

[6] M-H Chung, "On burst-and-coast swimming performance in fish-like locomotion", *Bioinspiration & Biomimetics*, vol. 4, 2009.

[7] J. Conte, Y. Modarres-Sadeghi, M.N. Watts., F.S. Hover and M.S. Triantafyllou, "A Fast-Starting Robotic Fish that Accelerates at $40~\mathrm{ms}^{-2}$", *Bioinspiration & Biomimetics*, vol. 5, 2010.

[8] V. Kopman, J. Laut, F. Acquaviva, A. Rizzo and M. Porfiri, "Dynamic modeling of a robotic fish propelled by a compliant tail", *IEEE Journal of Oceanic Engineering*, 2014.

[9] J. M. Gosline and M. E. DeMont, "Jet-propelled swimming squids", *Scientific American*, 252, 1985.

[10] P. S. Krueger and M. Gharib, "The significance of vortex ring formation to the impulse and thrust of starting jet", *Physics of Fluid*, vol. 15, pp. 12711281, 2003.

[11] P. S. Krueger, "An over-pressure correction to the slug model for vortex ring circulation", *Journal of Fluid Mechanics*, vol. 545, 2005.

[12] M. Krieg and K. Mohseni, "Modelling circulation, impulse and kinetic energy of starting jets with non-zero radial velocity", *Journal of Fluid Mechanics*, vol. 719, 2013.

[13] M. Krieg and K. Mohseni, "Thrust characterization of a bio-inspired vortex ring generator for locomotion of underwater robots", *IEEE Journal of Ocean Engineering*, vol. 33, 2008.

[14] A. A. Moslemi and P. S. Krueger, "Propulsive efficiency of a biomorphic pulsed-jet underwater vehicle", *Bioinspiration & Biomimetics*, vol. 5, 2010.

[15] L. A. Ruiz and R. W. Whittlesey and J. O. Dabiri, "Vortex-enhanced propulsion", *Journal of Fluid Mechanics*, vol. 668, 5-32, 2011.

[16] G. D. Weymouth and M. S. Trantafyllou, "Ultra-fast escape of a deformable jet-propelled body", *Journal of Fluid Mechanics*, vol. 721, pp. 367385, 2013.

[17] F. Giorgio Serchi, A. Arienti and C. Laschi, "An elastic pulsed-jet thruster for Soft Unmanned Underwater Vehicles" *IEEE International Conference on Robotics and Automation*, Karlsruhe, May 6-10, 2013.

[18] F. Giorgio Serchi, A. Arienti, C. Laschi, "Biomimetic Vortex Propulsion: Toward the New Paradigm of Soft Unmanned Underwater Vehicles" *Mechatronics, IEEE/ASME Transactions on* vol.18, no.2, pp. 484-493, April 2013.

[19] F. Giorgio Serchi, A. Arienti, C. Laschi, "A Soft Unmanned Underwater Vehicle with augmented thrust capability" *MTS/IEEE Proceedings Oceans*, San Diego, September 23-27, 2013.

[20] M. Giorelli, F. Giorgio Serchi and C. Laschi, "Forward speed control of a pulsed-jet soft-bodied underwater vehicle" *Proceedings of the MTS/IEEE OCEANS Conference*, San Diego, CA, USA, September, 21-27, 2013.

[21] F. Boyer, S. Ali, M. Porez "Macrocontinuous Dynamics for Hyperredundant Robots: Application to Kinematic Locomotion Bioinspired by Elongated Body Animals" *Robotics, IEEE Transactions on*, vol.28, no.2, pp.303,317, April 2012.

[22] F. Renda, M. Giorelli, M. Calisti, M. Cianchetti, C. Laschi, "Dynamic Model of a Multibending Soft Robot Arm Driven by Cables" *Robotics, IEEE Transactions on*, Vol 30, no 5, pp. 1109-1122, 2014.

[23] J. C. Simo and D. D. Fox, "On stress resultant geometrically exact shell model. Part I: formulation and optimal parametrization" *Journal Computer Methods in Applied Mechanics and Engineering* vol. 72, no. 3, pp. 267-304, Mar 1989.

[24] F. Renda, F. Boyer and C. Laschi, "Dynamic Model of a Jet-Propelled Soft Robot Inspired by the Octopus Mantle" *The International Conference on Biomimetics an Biohybrid Systems, Living Machine*, Milan, 30 Luglio - 1 Agosto, 2014.

[25] F. Renda, F. Giorgio-Serchi, F. Boyer and C. Laschi "Structural Dynamics of a Pulsed-Jet Propulsion System for Underwater Soft Robots" *Int J Adv Robot Syst*, vol. 12, no. 68, 2015.

[26] S. S. Antman, *Nonlinear Problems of Elasticity*, 2nd edn (Applied Mathematical Sciences vol 107) (New York:Springer), 2005.

[27] J. Linn, H. Lang and A. Tuganov, "Geometrically exact Cosserat rods with Kelvin-Voigt type viscous damping" *Mech. Sci.* vol 4., pp. 79-96, 2013.

[28] W. Johnson, P. D. Soden, and E. R. Trueman "A study in jet propulsion: an analysis of the motion of the squid, Loligo Vulgaris" Journal of Experimental Biology, vol. 56, pp. 155-165, 1972.

[29] F. Renda, F. Giorgio-Serchi, F. Boyer and C. Laschi "Locomotion and Elastodynamics Model of an Underwater Shell-like Soft Robot" *Robotics and Automation (ICRA), 2015 IEEE International Conference on*, pp.1158,1165, 26-30 May 2015, Seattle, USA, May 26-30, 2015.

[30] F. Boyer and A. Belkhiri "Reduced locomotion dynamics with passive internal DoF: application to nonholonomic and soft robotics" *Robotics, IEEE Transactions on*, vol.30, no.3, pp.578,592, June 2014.

[31] M. E. Gurtin, *An Introduction to Continuum Mechanics*, (Mathematics in Science and Engineering vol 158) (New York:Academic Press), 1981.